Multiobjective Optimization of Bespoke Gradient-Index Lenses: A Powerful Tool for Overcoming the Limitations of Transformation Optics

Jingwei Xu,[1,*] Eric B. Whiting,[1] Sawyer D. Campbell,[1] Pingjuan L. Werner,[1] Douglas H. Werner,[1] Jeremy A. Bossard,[2] John P. Barrett,[2] Joshua W. Withrow,[3] and James D. Weigner[3]

[1] *Department of Electrical Engineering, The Pennsylvania State University, University Park, Pennsylvania 16802, USA*

[2] *Rotary and Mission Systems, Lockheed Martin, Moorestown, New Jersey, USA*

[3] *Rotary and Mission Systems, Lockheed Martin, Syracuse, New York, USA*

(Received 30 September 2021; revised 5 May 2022; accepted 2 June 2022; published 8 August 2022)

Gradient-index (GRIN) lenses have paved the way for electromagnetic wave tailoring due to their spatially varying permittivities, which enable continuous manipulation of the wave as it passes through the lens volume. However, traditional GRIN design methodologies, such as transformation optics or geometrical optics, often generate lens profiles that are limited to single-band performance. Here, we propose a multiobjective optimization strategy customized for designing dual-band GRIN lenses. Utilizing this powerful inverse-design tool, in conjunction with an advanced manufacturing technique, a GRIN lens with compact size and nonintuitive permittivity distribution is designed, fabricated, and characterized. The lens is capable of realizing two unique gain enhancement objectives at the *L* and *C* bands simultaneously, where different feeding sources are employed at the two bands.

DOI: 10.1103/PhysRevApplied.18.024021

I. INTRODUCTION

Gradient-index (GRIN) lenses and metamaterials have long been an attractive topic due to the increased degrees of freedom they afford designers for manipulating the propagation of electromagnetic waves. Different from their homogeneous counterparts, where the wave-matter interaction is characterized at the interface between homogeneous materials, waves interact throughout the GRIN volume due to its spatially varying refractive-index profile. This enables one to tailor the behavior of electromagnetic waves as they propagate through the GRIN. The concept of GRIN metamaterials was proposed in Ref. [1], and they have been exploited to achieve a variety of functionalities, including focusing [2–8], beam steering [9–12], imaging [13–15], beam collimation [16], Bessel-beam generation [17], energy harvesting [5], and power transfer [18]. They also have applications in other fields such as acoustics [19,20].

Recently, there has been growing interest in GRIN lenses for directivity-enhancement applications [21–46] in a variety of areas, such as wireless communications. Many of the lenses published in the literature use a "phase-compensation" technique based on geometric optics (GO) [21–32,35,40]. Using this technique, the refractive-index distribution along the lens aperture is engineered so that a unique phase compensation is provided along the lens aperture to flatten the transmitted wave's phase front. Other types of GRIN profiles, such as the Luneburg lens [33,34,37,38] and half Maxwell fisheye lens [36,38], have seen numerous explorations by researchers for directivity enhancement. In addition to GO, transformation optics (TO) represents another powerful tool for creating GRIN lens designs [33,39,41–46]. Based on the invariance of Maxwell's equations under coordinate transformation, TO provides an opportunity to tailor the electromagnetic (EM) wave propagation. With TO, one can easily transform the cylindrical or spherical wave front of a source antenna into a planar wave front using a prescribed GRIN lens that captures the physics of the geometric transformation to realize a high-gain antenna.

Despite the advantages of these previous GRIN lenses, they have significant drawbacks. First, many experimentally realized lenses possess small effective refractive-index ranges, which limit their overall gain enhancement [22,26,37,40]. Other lenses have complex resonant unit-cell structures [21,27,35,36] that must be tuned to achieve the required effective permittivity. However, these metamaterial unit cells are intrinsically lossy, dispersive, and complicated to fabricate. Meanwhile, the advent of additive manufacturing [i.e., three-dimensional (3D) printing] has enabled a broader range of all-dielectric lenses, which are realized by printing negative inclusions (i.e., holes) within the lens to yield the required effective material

*jxx89@psu.edu

properties. Thus, significantly lower permittivity values can be achieved within a very small voxel compared to the base dielectric material. Due to the resolutions currently achievable with commercial 3D printers, additive manufacturing has a wide range of applications in both the rf [33,34] and terahertz [47] regimes.

Moreover, most literature examples operate at a single band, although some have realized relatively broadband performance [26,27,29,35,36,40]. Few of them, however, demonstrate multiband performance [24]. For metamaterial-based GRIN lenses, this is largely due to the inherent dispersion of unit-cell building blocks that comprise the lens. Therefore, the realization of broadband lenses often requires extra effort to carefully engineer the unit cell's dispersive behavior. For example, two types of unit cells were used in Ref. [29] to achieve large permittivity variation and reduce dispersion. Still, even with dispersionless materials, it is a nontrivial task to realize lenses that achieve unique gain-enhancement requirements across multiple-frequency bands. For example, TO is intrinsically a single-frequency transformation technique and, thus, fundamentally limited in its ability to realize multiband-lens solutions.

To overcome these challenges, we adopt a state-of-the-art multiobjective optimization strategy, which can directly optimize multiple unique directivity goals at different frequencies simultaneously while enforcing realistic material and fabrication constraints [48]. This procedure is applicable to lenses of any geometry and for arbitrary sources across multiple operational bands. In addition, it is not necessary to incorporate antireflection layers into the design process, such as in Ref. [23], since impedance matching is automatically considered as part of the optimization cost functions. Paired with a flexible GRIN profile generator, this optimization method is capable of realizing arbitrary and nonintuitive spatially varying permittivity profiles, which target multiband functionalities.

Here, we propose an inverse-design methodology that combines a free-form GRIN-profile-description technique with multiobjective optimization. We then report a dual-band compact-size GRIN lens, which achieves more than 4-dB and about-1-dB gain improvement compared to the source antenna alone across the L and C bands, respectively. The lens is fabricated using state-of-art additive manufacturing techniques and experimental far-field results are compared against simulated predictions. The proposed design approach is general and extendible to realize other GRIN devices with custom performance objectives.

II. DESIGN METHODOLOGY

Here, we aim to develop a GRIN lens that maximizes gain enhancement at the L band, while, at the same time, strives to achieve a transparent response (i.e., minimize the effect of the lens on gain) at the C band. Figure 1(a) shows the schematics of the dual-band lens concept, which is placed at some offset distance in front of the source. The source is switched between a 2×2 patch antenna array for the L band (1.2–1.4 GHz) and an 8×8 patch antenna array for the C band (5.2–5.9 GHz). Simulations are performed using COMSOL Multiphysics 5.4 (see additional information of the simulation setup in the Supplemental Material [49]).

Because the optimization is iterative, and the high-performance lens structures tend to be complicated, the design process can be extremely time-consuming. In our work, we adopt two methods to reduce computational burden. First, these realistic antenna sources are integrated into the simulation environment by capturing their radiated electric field distributions over a predefined aperture [see the red rectangular region in Fig. 1(b)], and then this spatially varying field is assigned to an excitation port within COMSOL [see the red rectangular region in Fig. 1(c)], which acts as an equivalent source in the lens simulation. This method is a flexible and efficient strategy, especially during optimizations, due to the fact that the time-consuming modeling of real source antennas is avoided. Please refer to the Supplemental Material [49] for additional details of the lens description.

Since the lens is electrically larger at the C band, direct full-wave simulation is computationally intensive. Therefore, we explore a simpler two-dimensional (2D) model in our simulations, as illustrated in Fig. 1(d). The simplification procedure is explained as follows: in the 2D model, the source field used corresponds to the center-cut line [the red line in Fig. 1(c)] of its original 3D counterpart, while the simulation domain used in the 2D model is the center-cut plane (i.e., X-Z plane) of the 3D domain. At each iteration

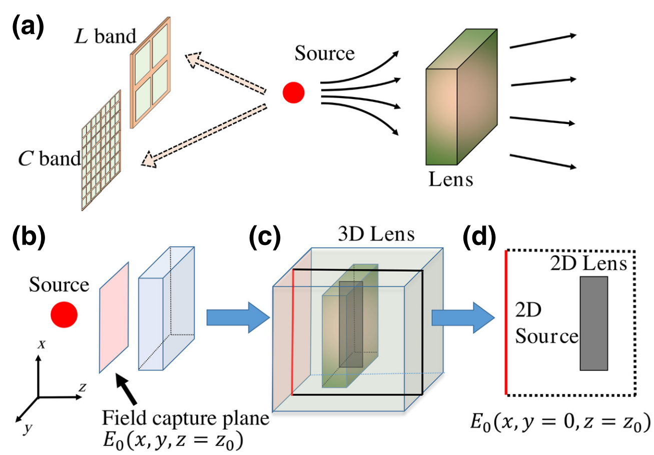

FIG. 1. (a) Gain-enhancement lens with dual-band patch antenna sources. (b) Field-capture plane used to import into the 2D solver. (c) 3D simulation domain using the equivalent source. (d) 2D simulation domain using the equivalent source.

during optimization, a 2D lens profile, $\varepsilon_r(x,z)$, is generated and simulated within the 2D domain. After optimization, a desired solution with gain improvement, ΔG^{2D}, is chosen according to the desired performance goals. Next, the lens profile of this desired solution, $\varepsilon_r^{2D}(x,z)_0$, is mapped to a 3D profile, $\varepsilon_r^{3D}(x,y=C,\ z)_0=\varepsilon_r^{2D}(x,\ z)_0$, where the lens permittivity is invariant along the y direction. The mapped 3D lens is able to increase the gain of the source antenna by ΔG^{3D} in the 3D domain.

After simulating the far-field gain of multiple randomly generated lenses, we find that there is a nearly proportional relationship between ΔG^{2D} and ΔG^{3D}. In other words, whenever the optimizer generates a solution with good gain improvement in the 2D domain, the mapped lens will have even higher gain improvement when simulated in the corresponding 3D domain (as expected). The link between the 2D and 3D domains is crucial to significantly reduce the computational burden of the simulations during optimization. Alternatively, deep-learning-assisted designs being explored by researchers [50,51] could further accelerate the optimization process.

A. Quasi-conformal transformation optics

To establish a baseline for multiband performance, let us first examine the performance of a traditional TO-derived GRIN lens. For simplicity, simulations are again performed in the 2D domain, as described above. Since the L-band performance is emphasized over that of the C band, we first design a lens based on the L-band source's wave front at 1.3 GHz. Figure 2(a) shows the air-filled virtual space defined by the region surrounded by a black-line contour, which is transformed into the physical space, as defined by the white rectangular region in Fig. 2(b). The permittivity distribution within the simulation domain is depicted in Fig. 2(b). Notice that the width of lens is fixed at 30 cm, as this is determined to be the best trade-off of size, weight, power, and required fabrication time. The TO lens is fed by the L-band (1.3 GHz) and C-band (5.55 GHz) 2D equivalent sources, and the corresponding near-field results are shown in Figs. 2(c) and 2(d), respectively. As expected, the lens performs well at the L band, and a more directive beam can be clearly observed. The lens increases the far-field gain of the source by 1.6 dB. At the C band, however, the lens negatively interacts with the incident wave and degrades the source gain by 1.5 dB and produces noticeable minor lobes. While this transformation is based on the source wave front at the L band, it is also possible to perform the transformation based on the C-band wavefront shape. Similar to Fig. 2(a), the virtual space shown in Fig. 2(e) is based on the wave front of the C-band source at 5.55 GHz. Notice that the shape of the virtual space is very similar to a rectangle, because the wave front is too flat. As expected, the permittivity distribution of the TO lens

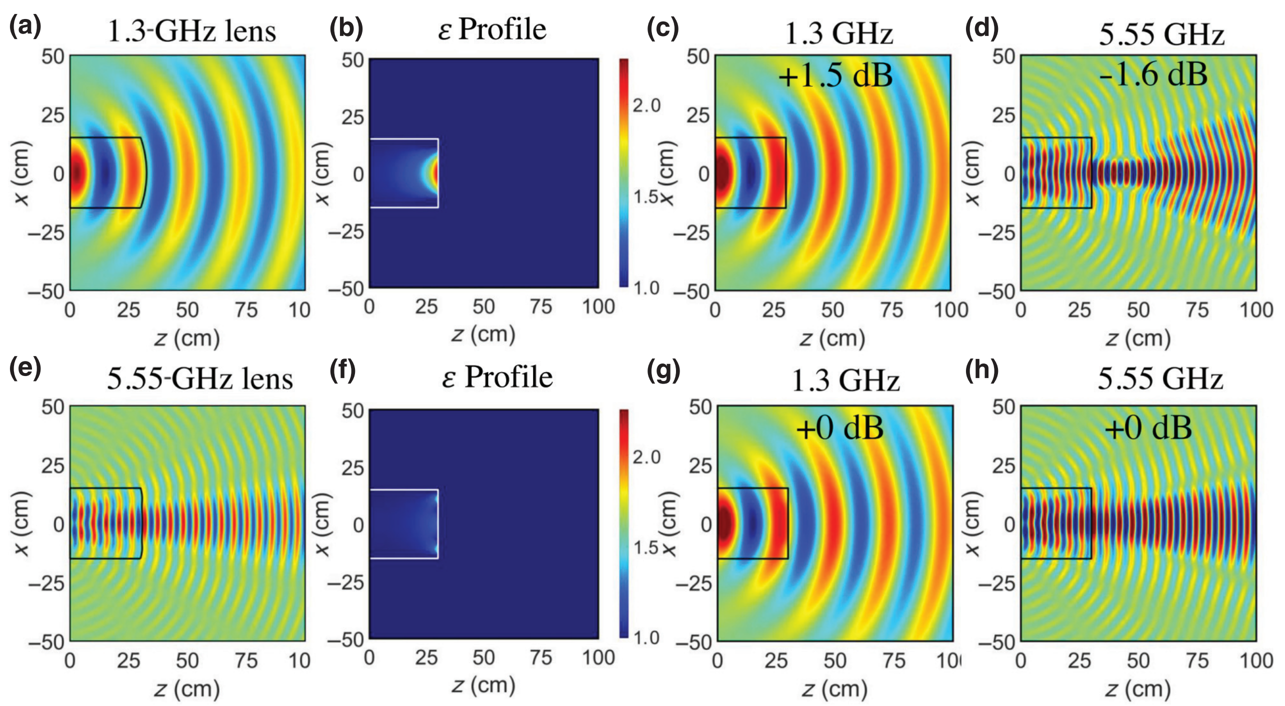

FIG. 2. Transformation optics lens. Virtual space of the TO lens targeted at (a) 1.3 GHz and (e) 5.55 GHz. (b),(f) Corresponding physical spaces and permittivity distributions of the TO lens. (c),(d),(g),(h) Simulated near field at 1.3 and 5.55 GHz using the lens profiles shown in (b),(f), respectively.

is close to homogeneous [see Fig. 2(f)], and the lens has a minimal influence on the radiation pattern in both bands, as shown in Figs. 2(g) and 2(h).

B. Multiobjective optimization strategy

The failure of TO is due to the fact that the source wave fronts are completely different at the L and C bands, since only a single wave front can be used for the geometrical transformation. Simply put, TO is a single-band transformation, which intrinsically precludes it from realizing multiband lenses, especially when there is a wide separation between the two bands. Here, we demonstrate that an optimization strategy can be utilized to effectively overcome this fundamental limitation. In the optical regime, multifrequency and multilens transformations are successfully realized using single-objective-optimization procedures [52]. However, since the L- and C-band objectives are not captured by geometrical transformations of any kind, a more general inverse-design approach must be implemented. Moreover, a successful strategy must pair nearly arbitrary GRIN-permittivity-profile generation with powerful global optimization to meet the desired multiband performance goals.

To this end, multiobjective optimization (MOO) is ideally suited for this problem due to its ability to simultaneously minimize multiple cost functions [53]. MOO is especially effective for hyperdimensional problems (i.e., ones with many input parameters) which are essentially impossible for humans to tune by hand. Unlike traditional single-objective optimizers, multiobjective algorithms present the user with a Pareto set of optimal solutions, which the designer can visualize to better understand the inherent trade-offs between all competing design objectives. When the optimization is finished, one has the freedom to choose the point along the Pareto front to best represent the compromise between the competing goals. This flexibility enabled by MOO is very important for our problem, where one objective needs to be prioritized over the other. Within the optics and electromagnetics communities, MOO has seen tremendous success in the synthesis of a wide range of metadevices [54–56].

For this problem, we define two objectives, $o1$ and $o2$, which denote the minimum gain enhancement across the L and C bands, respectively:

$$o1 = -\min\{G^{2D}_{f(i)} - G^{2D}_{0,f(i)}\} = -\Delta G^{2D}_{l}, \quad i = 1, 2, 3, \tag{1a}$$

$$o2 = -\min\{G^{2D}_{f(i)} - G^{2D}_{0,f(i)}\} = -\Delta G^{2D}_{c}, \quad i = 4, 5, 6, \tag{1b}$$

where $f(1) = 1.2$ GHz, $f(3) = 1.3$ GHz, $f(3) = 1.4$ GHz, $f(4) = 5.2$ GHz, $f(5) = 5.55$ GHz, and $f(6) = 5.9$ GHz; $G^{2D}_{f(i)}$ and $G^{2D}_{0,f(i)}$ denote the broadside gain values at $f(i)$ with and without a lens, respectively.

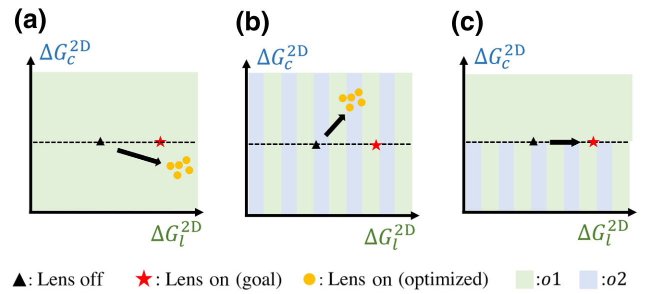

FIG. 3. Schematics of the proposed multiobjective optimization strategy, where (a) only L-band gain is optimized and (b) both L band and C band are optimized. (c) Different goals are considered when C-band gain changes.

What complicates this problem is that the gain enhancement required at the two bands is "unbalanced." If only $o1$ is considered, then the lens performance at the C band cannot be guaranteed. A large amount of time would be spent on searching solutions that potentially bring undesirable gain degradation at the C band, which is not efficient [see Fig. 3(a)]. However, if both $o1$ and $o2$ are considered, the optimizer tends to find solutions that perform equally well at both frequency bands, which is not desired either, since we essentially want the lens to be transparent (i.e., no impact to the far field) across the C band [see Fig. 3(b)]. To address this, we introduce the "C-band threshold gain," $\Delta G^{2D}_{c,0} = 0$. When the gain improvement at the C band is less than 0 dB (i.e., $\Delta G^{2D}_{c} < 0$), both $o1$ and $o2$ are considered. However, when $\Delta G^{2D}_{c} > 0$, then only $o1$ is considered. With this approach, the problem of the unbalanced need for gain improvement at the two bands is overcome. Accordingly, the objective function $o2$ can be modified as

$$o2' = o2, \text{ if } o2 \geq 0; o2' = 0, \text{ if } o2 < 0. \tag{2}$$

At each iteration during optimization, a new lens profile, in the form of a 2D Bézier surface [57], is generated. The topology of this surface is governed by a set of $m \times n$ control points, the values of which float within a predefined range corresponding to the chosen permittivity range to be used during fabrication. With the control-surface description, the lens-permittivity profile is nearly free-form and can assume highly irregular and unconventional patterns. Please see the Supplemental Material [49] for more details of lens-profile generations. This lens profile is imported into COMSOL using MATLAB and the far-field radiation

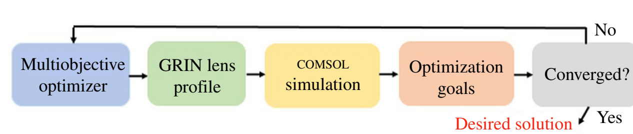

FIG. 4. Flowchart of the multiobjective optimization process.

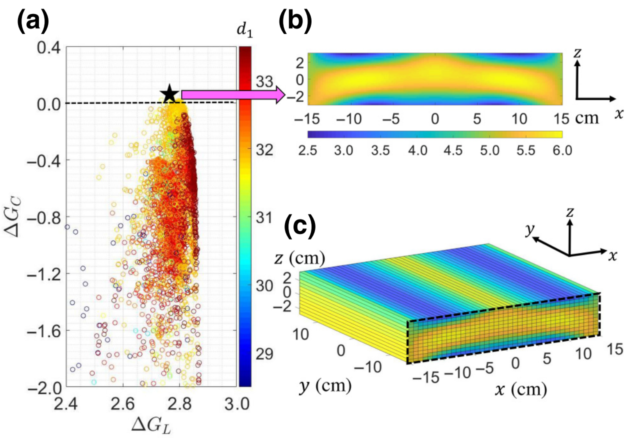

FIG. 5. (a) Scatter plot of the multiobjective optimization. The x and y axes correspond to minimum gain enhancement across L band and C band, and the color bar represents offset distance between lens and source d_1. Black star corresponds to the optimal solution. (b) 2D permittivity profile of the optimal solution. (c) 3D profile of the optimal solution.

pattern of the system (i.e., source + lens) is calculated and fed back to the optimizer. These results are used by the optimizer to intelligently choose the next set of samples, as it attempts to minimize the multiple cost functions. This process continues until the results are converged, as Fig. 4 shows.

III. OPTIMIZED DESIGN

After several rounds of optimizations with different lens geometries and permittivity ranges, a 30-cm-wide by 6-cm-thick lens with permittivity range $\varepsilon_r = 2.52 - -5.94$ is chosen, as it represents the best trade-off between fabrication cost or complexity and dual-band performance. The MOO results clearly show the trade-off between the far-field performances at the L and C bands [see Fig. 5(a)]. Each circle represents a unique GRIN lens solution, with a distinct permittivity profile and an offset distance from the source. The black dashed line corresponds to the threshold gain, $\Delta G^{2\mathrm{D}}_{c,0} = 0$. The solutions mostly occupy the spaces below this threshold, which indicates that the optimizer does not "waste" time searching for solutions that lead to very large ΔG_{c} values. These results prove the efficacy of the proposed optimization strategy.

An optimal solution is taken from the MOO Pareto set, as indicated by the black star, which has $\Delta G^{2\mathrm{D}}_{l} = 2.8$ and $\Delta G^{2\mathrm{D}}_{c} = 0.1$. The permittivity profile is shown in Fig. 5(b). One can observe that the lens has lower permittivity values near its bottom and upper boundaries, which are consequential in minimizing reflections. For fabrication and

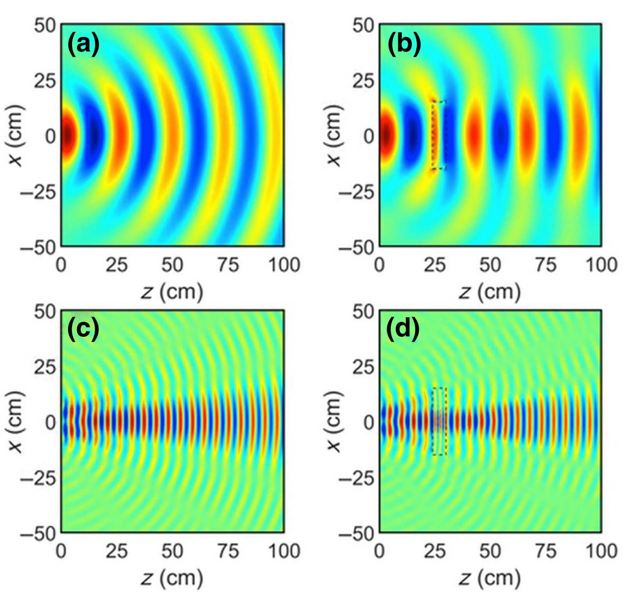

FIG. 6. Simulated near-field results for lens *off* (left) and lens *on* (right) cases at (a),(b) 1.3 GHz and (c),(d) 5.55 GHz.

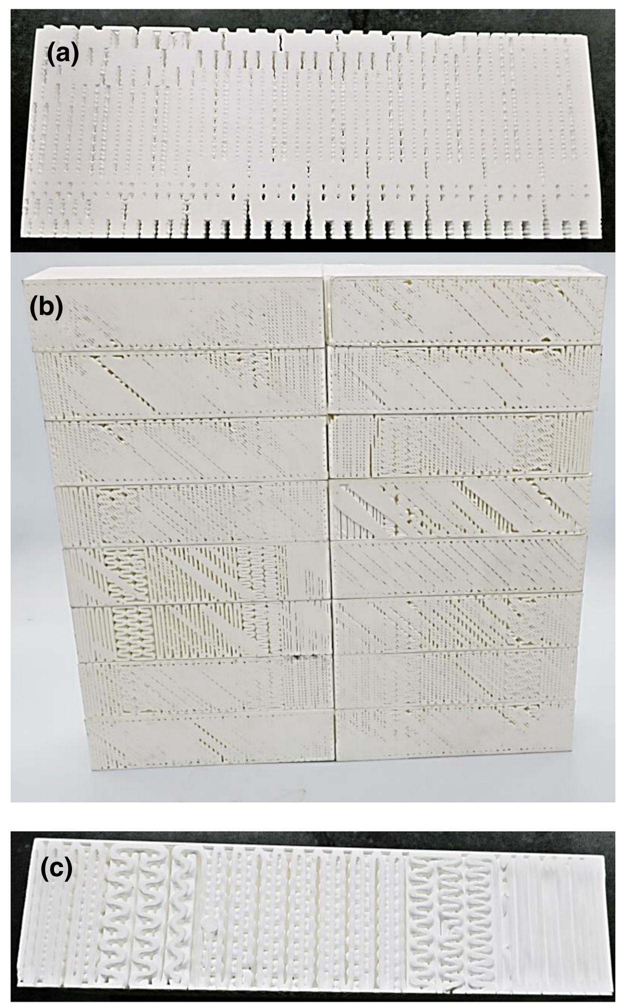

FIG. 7. Photographs of the fabricated lens prototype (a),(c). Different views of an individual brick (b). Bottom view of the GRIN lens.

testing, the 2D profile is mapped to 3D [see Fig. 5(c)], as described in Sec. II. The 3D lens is invariant along the y direction, and its X-Z cut is exactly the 2D profile, as the black dashed rectangle shows. Notice that the continuous profile is discretized into small voxels ($7.5 \times 5\ \mathrm{mm}^2$), which correspond to the minimum feature-size constraints of the 3D printer.

Figure 6 shows the simulated near-field distribution around the GRIN lens. For simplicity, the simulation is performed in the 2D domain [see Fig. 2(d)] rather than in the 3D domain. At the L band, we can clearly observe that the quasi-cylindrical wave front is flattened to nearly planar by the GRIN lens, while, at the C band, the near-field pattern is minimally perturbed by the lens, especially in the broadside direction.

IV. LENS FABRICATION AND EXPERIMENTAL RESULTS

The chosen lens is converted to a format readable by the 3D printer and fabricated using alumina. The permittivity is precisely controlled by adjusting the size of negative inclusions within the lens (i.e., holes), which serve to lower the permittivity of the base alumina material. Figure 7 shows images of the fabricated lens. The GRIN profile can be seen in the holey pattern observed on the lens surface.

This fabricated lens is measured by Lockheed Martin at their on-site spherical near-field anechoic chamber, see Fig. 8. The sources and lens are placed near the center of the chamber using a combination of combiners to feed the source. Low-dielectric-constant foam ($\varepsilon_r \approx 1.03$) is used to place the lens in relation to the sources, ensuring that the lens is the same distance from the L-band and C-band sources. Figures 9(a), 9(b), 9(d), and 9(e) show the realized gain patterns in both the X-Z plane (i.e., the elevation plane) and Y-Z plane (i.e., the azimuth plane). At the L band, the broadside gain of the source plus GRIN lens is more than 4 dB higher than the source alone. Notice that this number is, as expected, larger than the results from optimizations, which are performed using 2D models. Simulated and experimental results agree very well, especially at small θ angles. There is around a 5° shift between the

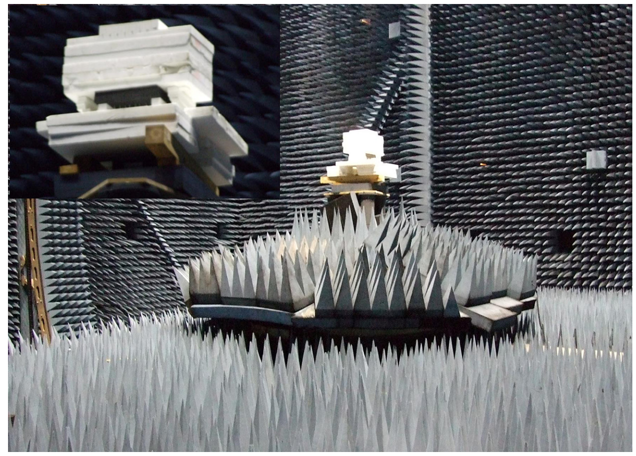

FIG. 8. Photograph of the anechoic chamber during measurement (inset shows a close up of the lens prototype).

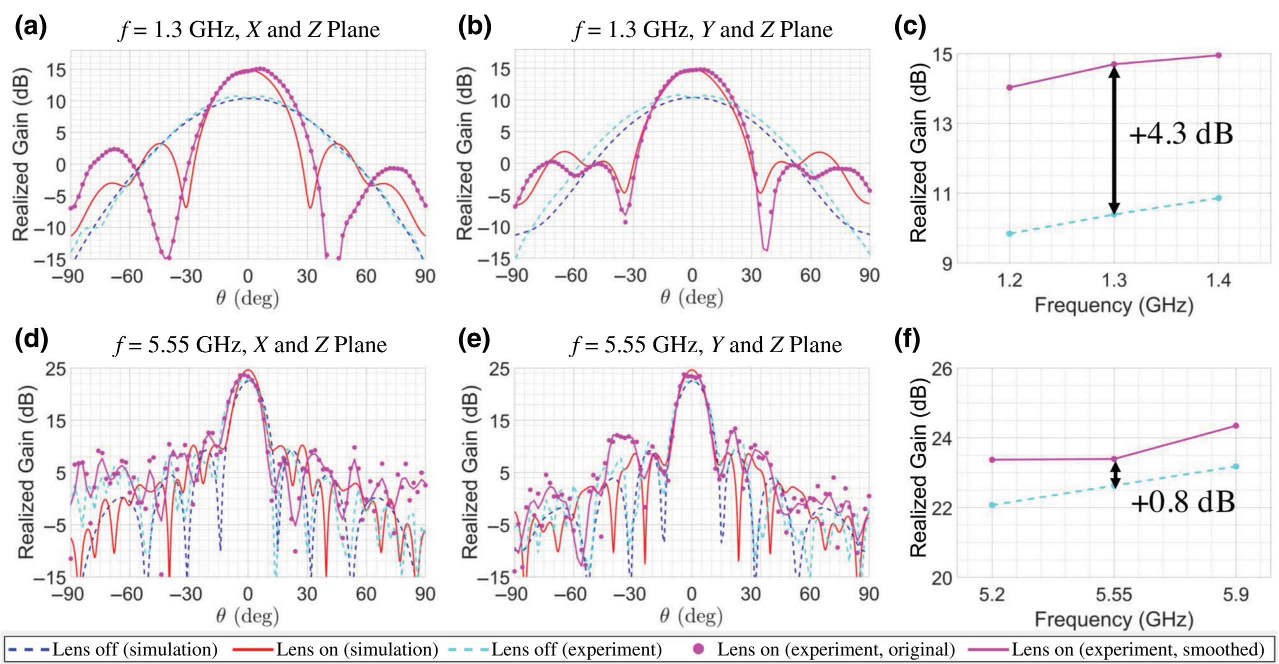

FIG. 9. Simulated and measured X-Z plane and Y-Z plane realized gain patterns of the patch antenna for lens *off* and lens *on* cases at (a),(b) 1.3 GHz and (d),(e) 5.55 GHz. Broadside-realized gain versus frequency across (c) L band and (f) C band.

peak gain positions, which is caused by a combination of misalignments between the source, lens, and receiving antenna in the measurement setup and phase variance at the source based on the tolerances of the combiner network required to feed the array. At the *C* band, the gain of the source plus GRIN lens is around 0.8 dB higher than the source alone. While some discrepancies between the peak gain and minor-lobe positions can be observed, the overall agreement between the simulated and measured performances is quite good. Figures 9(c) and 9(f) show the broadside gain as a function of frequency across the *L* and *C* bands, respectively.

V. CONCLUSION

In this paper, a dual-band GRIN lens design with an nonintuitive permittivity distribution is optimized, fabricated, and experimentally validated. The lens prototype achieves a highly directive radiation pattern at the *L* band with more than 4-dB gain improvement, while leading to around 1-dB gain improvement at the *C* band. Excellent agreement between the measured and simulated far-field patterns is observed. This bespoke lens significantly outperforms its conventional transformation optics counterpart. Moreover, this paper demonstrates that a compact size lens ($1.3\lambda_0 \times 0.26\lambda_0$, where λ_0 is the central wavelength at the *L* band) can operate with two distinct far-field performance goals at two widely separated frequency bands. The proposed flexible and versatile optimization strategy not only opens an avenue to synthesize high-gain GRIN lenses, but also a wide range of other lens antennas with diverse functionalities.

ACKNOWLEDGMENTS

This work is funded, in part, by Lockheed Martin Corporation.

[1] D. R. Smith, J. J. Mock, A. F. Starr, and D. Schurig, Gradient index metamaterials, Phys. Rev. E **71**, 036609 (2005).

[2] S.-G. Park, K. Lee, D. Han, J. Ahn, and K.-H. Jeong, Subwavelength silicon through-hole arrays as an all-dielectric broadband Terahertz gradient index metamaterial, Appl. Phys. Lett. **105**, 091101 (2014).

[3] P. R. West, J. L. Stewart, A. V. Kildishev, V. M. Shalaev, V. V. Shkunov, F. Strohkendl, Y. A. Zakharenkov, R. K. Dodds, and R. Byren, All-dielectric subwavelength metasurface focusing lens, Opt. Express **22**, 26212 (2014).

[4] A. Dhouibi, S. N. Burokur, A. de Lustrac, and A. Priou, Compact metamaterial-based substrate-integrated Luneburg lens antenna, IEEE Antennas Wirel. Propag. Lett. **11**, 1504 (2012).

[5] A. Zareei, A. Darabi, M. J. Leamy, and M.-R. Alam, Continuous profile flexural GRIN lens: Focusing and harvesting flexural waves, Appl. Phys. Lett. **112**, 023901 (2018).

[6] O. Paul, B. Reinhard, B. Krolla, R. Beigang, and M. Rahm, Gradient index metamaterial based on slot elements, Appl. Phys. Lett. **96**, 241110 (2010).

[7] R. B. Greegor, C. G. Parazzoli, J. A. Nielsen, M. A. Thompson, M. H. Tanielian, and D. R. Smith, Simulation and testing of a graded negative index of refraction lens, Appl. Phys. Lett. **87**, 091114 (2005).

[8] Y.-Y. Zhao, Y.-L. Zhang, M.-L. Zheng, X.-Z. Dong, X.-M. Duan, and Z.-S. Zhao, Three-dimensional Luneburg lens at optical frequencies: Three-dimensional Luneburg lens at optical frequencies, Laser Photonics Rev. **10**, 665 (2016).

[9] H. F. Ma, X. Chen, H. S. Xu, X. M. Yang, W. X. Jiang, and T. J. Cui, Experiments on high-performance beam-scanning antennas made of gradient-index metamaterials, Appl. Phys. Lett. **95**, 094107 (2009).

[10] N. Kundtz and D. R. Smith, Extreme-angle broadband metamaterial lens, Nat. Mater. **9**, 129 (2010).

[11] A. Dhouibi, S. N. Burokur, and A. de Lustrac, Planar metamaterial-based beam-scanning broadband microwave antenna, J. Appl. Phys. **115**, 194901 (2014).

[12] H. F. Ma, G. Z. Wang, W. X. Jiang, and T. J. Cui, Independent control of differently-polarized waves using anisotropic gradient-index metamaterials, Sci. Rep. **4**, 6337 (2015).

[13] J. Knittel, L. Schnieder, G. Buess, B. Messerschmidt, and T. Possner, Endoscope-compatible confocal microscope using a gradient index-lens system, Opt. Commun. **188**, 267 (2001).

[14] S. Ji, M. Ponting, R. S. Lepkowicz, A. Rosenberg, R. Flynn, G. Beadie, and E. Baer, A bio-inspired polymeric gradient refractive index (GRIN) human eye lens, Opt. Express **20**, 26746 (2012).

[15] W. Jung, W. Benalcazar, A. Ahmad, U. Sharma, H. Tu, and S. A. Boppart, Numerical analysis of gradient index lens–based optical coherence tomography imaging probes, J. Biomed. Opt. **15**, 066027 (2010).

[16] Q. Wu, Z. H. Jiang, O. Quevedo-Teruel, J. P. Turpin, W. Tang, Y. Hao, and D. H. Werner, Transformation optics inspired multibeam lens antennas for broadband directive radiation, IEEE Trans. Antennas Propag. **61**, 5910 (2013).

[17] M. Qing Qi, W. X. Tang, and T. J. Cui, A broadband Bessel beam launcher using metamaterial lens, Sci. Rep. **5**, 11732 (2015).

[18] A. K. Baghel, S. S. Kulkarni, and S. K. Nayak, Far-field wireless power transfer using GRIN lens metamaterial at GHz frequency, IEEE Microw. Wirel. Compon. Lett. **29**, 424 (2019).

[19] A. Climente, D. Torrent, and J. Sánchez-Dehesa, Sound focusing by gradient index sonic lenses, Appl. Phys. Lett. **97**, 104103 (2010).

[20] D. Li, L. Zigoneanu, B.-I. Popa, and S. A. Cummer, Design of an acoustic metamaterial lens using genetic algorithms, J. Acoust. Soc. Am. **132**, 2823 (2012).

[21] E. Erfani, M. Niroo-Jazi, and S. Tatu, A high-gain broadband gradient refractive index metasurface lens antenna, IEEE Trans. Antennas Propag. **64**, 1968 (2016).

[22] F.-Y. Meng, R.-Z. Liu, K. Zhang, D. Erni, Q. Wu, L. Sun, and J. L.-W. Li, Automatic design of broadband gradient

index metamaterial lens for gain enhancement of circularly polarized antennas, Prog. Electromagn. Res. **141**, 17 (2013).

[23] N. Zhang, W. X. Jiang, H. F. Ma, W. X. Tang, and T. J. Cui, Compact high-performance lens antenna based on impedance-matching gradient-index metamaterials, IEEE Trans. Antennas Propag. **67**, 1323 (2019).

[24] M. K. T. Al-Nuaimi, Wei Hong, and Yan Zhang, Design of high-directivity compact-size conical horn lens antenna, IEEE Antennas Wirel. Propag. Lett. **13**, 467 (2014).

[25] H. Zhu, S. W. Cheung, and T. I. Yuk, Enhancing antenna boresight gain using a small metasurface lens: Reduction in half-power beamwidth, IEEE Antennas Propag. Mag. **58**, 35 (2016).

[26] R. Singha and D. Vakula, Gain enhancement of the ultra-wideband tapered slot antenna using broadband gradient refractive index metamaterial, Int. J. RF Microw. Comput.-Aided Eng. **28**, e21191 (2018).

[27] H.-X. Xu, G.-M. Wang, Z. Tao, and T. J. Cui, High-directivity emissions with flexible beam numbers and beam directions using gradient-refractive-index fractal metamaterial, Sci. Rep. **4**, 5744 (2015).

[28] Q. L. Li, S. W. Cheung, D. Wu, and T. I. Yuk, Microwave lens using periodic dielectric sheets for antenna-gain enhancement, IEEE Trans. Antennas Propag. **65**, 2068 (2017).

[29] Z. Yang, L. Guo, C. Yao, Q. Zhang, Z. Xu, M. Guo, and Z. Wang, Ultrawideband antipodal tapered slot antenna with gradient refractive index metamaterial lens, IEEE Antennas Wirel. Propag. Lett. **18**, 2741 (2019).

[30] J. H. Kim, C.-H. Ahn, and J.-K. Bang, Antenna gain enhancement using a holey superstrate, IEEE Trans. Antennas Propag. **64**, 1164 (2016).

[31] K. Chen, Z. Yang, Y. Feng, B. Zhu, J. Zhao, and T. Jiang, Improving microwave antenna gain and bandwidth with phase compensation metasurface, AIP Adv. **5**, 067152 (2015).

[32] X. Chen, H. Feng Ma, X. Ying Zou, W. Xiang Jiang, and T. Jun Cui, Three-dimensional broadband and high-directivity lens antenna made of metamaterials, J. Appl. Phys. **110**, 044904 (2011).

[33] C. Mateo-Segura, A. Dyke, H. Dyke, S. Haq, and Y. Hao, Flat Luneburg lens via transformation optics for directive antenna applications, IEEE Trans. Antennas Propag. **62**, 1945 (2014).

[34] M. Liang, W.-R. Ng, K. Chang, K. Gbele, M. E. Gehm, and H. Xin, A 3-D Luneburg lens antenna fabricated by polymer jetting rapid prototyping, IEEE Trans. Antennas Propag. **62**, 1799 (2014).

[35] H. W. Tian, W. X. Jiang, X. Li, Z. P. Chen, and T. J. Cui, An ultra-wideband and high-gain antenna based on three-dimensional impedance-matching metamaterial lens, IEEE Trans. Antennas Propag. **69**, 3084 (2021).

[36] H.-X. Xu, G.-M. Wang, Z. Tao, and T. Cai, An octave-bandwidth half Maxwell fish-eye lens antenna using three-dimensional gradient-index fractal metamaterials, IEEE Trans. Antennas Propag. **62**, 4823 (2014).

[37] F. Fan, M. Cai, J. Zhang, Z. Yan, and J. Wu, Wideband low-profile Luneburg lens based on a glide-symmetric metasurface, IEEE Access **8**, 85698 (2020).

[38] J. Chen, Y. Zhao, L. Xing, Z. He, and L. Sun, Broadband bifunctional Luneburg–fisheye lens based on anisotropic metasurface, Sci. Rep. **10**, 20381 (2020).

[39] T. Ding, J. Yi, H. Li, H. Zhang, and S. N. Burokur, 3D field-shaping lens using all-dielectric gradient refractive index materials, Sci. Rep. **7**, 782 (2017).

[40] R. Singha and D. Vakula, Directive beam of the monopole antenna using broadband gradient refractive index metamaterial for ultra-wideband application, IEEE Access **5**, 9757 (2017).

[41] J. P. Turpin, Q. Wu, D. H. Werner, B. Martin, M. Bray, and E. Lier, Low cost and broadband dual-polarization metamaterial lens for directivity enhancement, IEEE Trans. Antennas Propag. **60**, 5717 (2012).

[42] A. Keivaan, M. H. Fakheri, A. Abdolali, and H. Oraizi, Design of coating materials for cloaking and directivity enhancement of cylindrical antennas using transformation optics, IEEE Antennas Wirel. Propag. Lett. **16**, 3122 (2017).

[43] Z. H. Jiang, M. D. Gregory, and D. H. Werner, Broadband high directivity multibeam emission through transformation optics-enabled metamaterial lenses, IEEE Trans. Antennas Propag. **60**, 5063 (2012).

[44] J. Yi, S. N. Burokur, G.-P. Piau, and A. de Lustrac, 3D printed broadband transformation optics based all-dielectric microwave lenses, J. Opt. **18**, 044010 (2016).

[45] J. Yi, S. N. Burokur, G.-P. Piau, and A. de Lustrac, Coherent beam control with an all-dielectric transformation optics based lens, Sci. Rep. **6**, 18819 (2016).

[46] M. Ebrahimpouri and O. Quevedo-Teruel, Bespoke lenses based on quasi-conformal transformation optics technique, IEEE Trans. Antennas Propag. **65**, 2256 (2017).

[47] F. Zhou, W. Cao, B. Dong, T. Reissman, W. Zhang, and C. Sun, Additive manufacturing of a 3D terahertz gradient-refractive index lens, Adv. Opt. Mater. **4**, 1034 (2016).

[48] S. D. Campbell, D. Sell, R. P. Jenkins, E. B. Whiting, J. A. Fan, and D. H. Werner, Review of numerical optimization techniques for meta-device design [invited], Opt. Mater. Express **9**, 1842 (2019).

[49] See the Supplemental Material at http://link.aps.org/supplemental/10.1103/PhysRevApplied.18.024021 for details of the lens-profile generation, source description, and simulation setup.

[50] Z. Huang, X. Liu, and J. Zang, The inverse design of structural color using machine learning, Nanoscale **11**, 21748 (2019).

[51] R. Yan, T. Wang, X. Jiang, Q. Zhong, X. Huang, L. Wang, and X. Yue, Design of high-performance plasmonic nanosensors by particle swarm optimization algorithm combined with machine learning, Nanotechnology **31**, 375202 (2020).

[52] S. D. Campbell, J. Nagar, and D. H. Werner, Multi-element, multi-frequency lens transformations enabled by optical wavefront matching, Opt. Express **25**, 17258 (2017).

[53] K. Deb and K. Deb, in *Search Methodologies*, edited by E. K. Burke and G. Kendall (Springer, US, Boston, MA, 2014), pp. 403–449.

[54] J. A. Easum, J. Nagar, P. L. Werner, and D. H. Werner, Efficient multiobjective antenna optimization with tolerance

analysis through the use of surrogate models, IEEE Trans. Antennas Propag. **66**, 6706 (2018).

[55] J. Nagar, S. D. Campbell, Q. Ren, J. A. Easum, R. P. Jenkins, and D. H. Werner, Multiobjective optimization-aided metamaterials-by-design with application to highly directive nanodevices, IEEE J. Multiscale Multiphysics Comput. Tech. **2**, 147 (2017).

[56] D. Z. Zhu, P. L. Werner, and D. H. Werner, Design and optimization of 3-D frequency-selective surfaces based on a multiobjective lazy ant colony optimization algorithm, IEEE Trans. Antennas Propag. **65**, 7137 (2017).

[57] P. E. Sieber and D. H. Werner, Infrared broadband quarter-wave and half-wave plates synthesized from anisotropic Bézier metasurfaces, Opt. Express **22**, 32371 (2014).